Since January 2020 Elsevier has created a COVID-19 resource centre with free information in English and Mandarin on the novel coronavirus COVID-19. The COVID-19 resource centre is hosted on Elsevier Connect, the company's public news and information website.

blood®
Regular Article

PHAGOCYTES, GRANULOCYTES, AND MYELOPOIESIS

Resolvin T-series reduce neutrophil extracellular traps

Nan Chiang,[1] Miyuki Sakuma,[2] Ana R. Rodriguez,[3] Bernd W. Spur,[3] Daniel Irimia,[2] and Charles N. Serhan[1]

[1]Center for Experimental Therapeutics and Reperfusion Injury, Department of Anesthesiology, Perioperative and Pain Medicine, Brigham and Women's Hospital and Harvard Medical School, Boston, MA; [2]BioMEMS Resource Center, Center for Engineering in Medicine and Surgical Services, Massachusetts General Hospital, Shriners Hospitals for Children, and Harvard Medical School, Boston, MA; and [3]Department of Cell Biology and Neuroscience, Rowan University-SOM, Stratford, NJ

KEY POINTS

- RvTs reduce NETs in human whole blood and murine *S aureus* infections using novel microfluidic NET-capturing devices.
- RvTs enhance macrophage NET clearance, offering a new resolution mechanism for infections and coagulopathies.

The newly identified 13-series (T-series) resolvins (RvTs) regulate phagocyte functions and accelerate resolution of infectious inflammation. Because severe acute respiratory syndrome coronavirus 2 elicits uncontrolled inflammation involving neutrophil extracellular traps (NETs), we tested whether stereochemically defined RvTs regulate NET formation. Using microfluidic devices capturing NETs in phorbol 12-myristate 13-acetate–stimulated human whole blood, the RvTs (RvT1-RvT4; 2.5 nM each) potently reduced NETs. With interleukin-1β–stimulated human neutrophils, each RvT dose and time dependently decreased NETosis, conveying ~50% potencies at 10 nM, compared with a known NETosis inhibitor (10 μM). In a murine *Staphylococcus aureus* infection, RvTs (50 ng each) limited neutrophil infiltration, bacterial titers, and NETs. In addition, each RvT enhanced NET uptake by human macrophages; RvT2 was the most potent of the four RvTs, giving a >50% increase in NET-phagocytosis. As part of the intracellular signaling mechanism, RvT2 increased cyclic adenosine monophosphate and phospho–AMP-activated protein kinase (AMPK) within human macrophages, and RvT2-stimulated NET uptake was abolished by protein kinase A and AMPK inhibition. RvT2 also stimulated NET clearance by mouse macrophages in vivo. Together, these results provide evidence for novel pro-resolving functions of RvTs, namely reducing NETosis and enhancing macrophage NET clearance via a cyclic adenosine monophosphate–protein kinase A–AMPK axis. Thus, RvTs open opportunities for regulating NET-mediated collateral tissue damage during infection as well as monitoring NETs.

Introduction

Excessive uncontrolled inflammation is a critical component of many prevalent diseases potentially arising from failed resolution mechanisms.[1,2] In several cases, novel pro-resolving mediators can rescue and resolve excessive inflammation (eg, arthritis,[3] pain,[4] periodontitis,[5] cancer,[6] and cardiovascular diseases[7,8]), as well as bacterial and viral infections[9] such as the recent severe acute respiratory syndrome coronavirus 2 (SARS-CoV-2) infection.[10,11] It was therefore deemed important to elucidate the cellular and molecular mechanisms controlling resolution of the acute inflammatory response.[12-14] Resolution of the acute inflammatory response is now widely recognized as an active process, temporally and spatially governed by cellular and molecular events that include the biosynthesis of a superfamily of endogenous pro-resolving lipid mediators that act on phagocytes and the innate immune system.[12] D-series resolvins (RvDs), protectins, and maresins are among these and biosynthesized from docosahexaenoic acid (reviewed elsewhere[15]). These potent molecules belong to the superfamily of specialized pro-resolving mediators (SPMs) because they possess potent stereoselective anti-inflammatory, pro-resolving, and organ-protective actions in the picogram to nanogram ranges.[15] They are specialized to limit neutrophil infiltration,[14] reduce pain,[4] enhance innate host defense,[2,16] and contribute to catabasis in tissue repair and regeneration.[5,12,17,18]

While investigating endogenous resolution of inflammation mechanisms, we encountered an entirely new series of resolvins that use n-3 docosapentaenoic acid as a precursor, termed the 13-series resolvins (RvTs)[19] because of their unique structures (ie, a hydroxyl group on the carbon-13 position), biosynthesis, and novel bioactions. These resolvins include 4 distinct bioactive molecules (RvT1, RvT2, RvT3, and RvT4) found in mouse infectious exudates and also produced by human cells and blood. Each of the RvT members identified to date is a potent agonist of pro-resolving phagocyte functions that accelerates resolution, increases survival in *Escherichia coli* infection, and controls inflammatory arthritis.[19,20] These findings provide a molecular basis for appreciating the critical roles of the innate response in clearing infection via active resolution.[21] Recently, the total organic synthesis of the main RvTs was achieved[22,23]; specifically, RvT1, 7S,13R,20S-trihydroxy-8E,10Z,14E,16Z,18E-docosapentaenoic acid; RvT2, 7S,12R,13S-trihydroxy-8Z,10E,14E,16Z,19Z-docosapentaenoic acid; RvT3, 7S,8R,13S-trihydroxy-9E,11E,14E,16Z,19Z-docosapentaenoic acid; and RvT4, 7S,13R-dihydroxy-8E,10Z,14E,16Z,19Z-docosapentaenoic acid. These

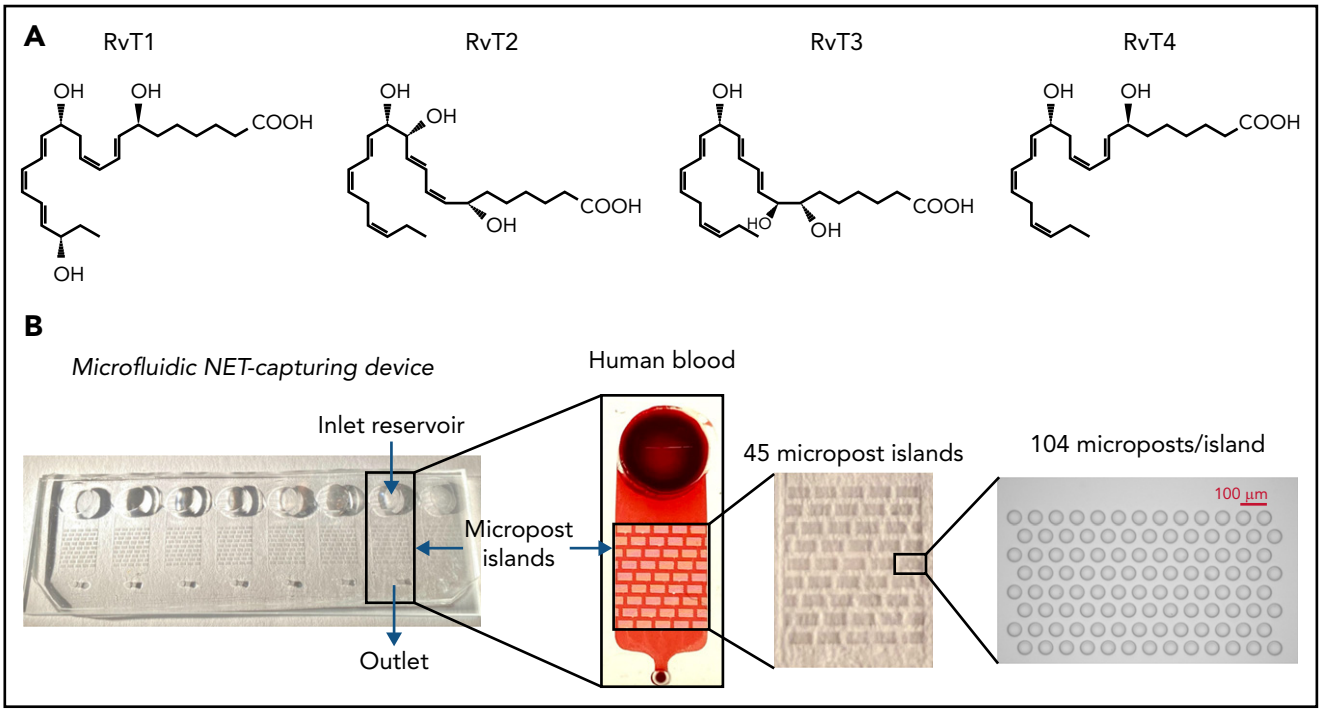

Figure 1. The microfluidic device for trapping NETs in human blood. (A) Structures of RvTs used in these experiments. RvT1: 7S,13R,20S-trihydroxy-8E,10Z,14E,16Z,18E-docosapentaenoic acid; RvT2: 7S,12R,13S-trihydroxy-8Z,10E,14E,16Z,19Z-docosapentaenoic acid; RvT3: 7S,8R,13S-trihydroxy-9E,11E,14E,16Z,19Z-docosapentaenoic acid; and RvT4: 7S,13R- dihydroxy-8E,10Z,14E,16Z,19Z-docosapentaenoic acid. (B) Overview of the microfluidic NET-capturing device. Each device consists of an inlet reservoir (for loading samples [eg, human blood]), micropost islands (for capturing NETs), and an outlet connected via Tygon Tubing to a syringe pump; flow rate was set at 10 μL/min with a target volume of 50 μL. The scheme illustrates a device in the absence or presence of human blood. Each device contains 45 micropost islands, and each island is formed by an array of 104 microposts.

findings taken together underscore the diverse structures of this 13-series of resolvins and their potential.

Neutrophils are the first line of cellular defense against invading pathogens.[14,24] They possess both intracellular antimicrobial activities via phagocytosis, mostly within phagolysosomes, and extracellular activities via release of neutrophil extracellular traps (NETs) that can trap microbes.[25] Excessive NETs are also recognized as a source of collateral tissue damage in disease pathologies.[26-31] NETs have a critical role in bacterial and viral infections, as in SARS-CoV-2 infections,[32] and excessive NETosis, namely the process of NET formation, can lead to coagulopathies observed in many patients with coronavirus disease 2019 (COVID-19).[33-35] Acute respiratory distress syndrome (ARDS) is also associated with defective clearance of NETs by macrophages (MΦs).[36] Hence, reducing NETosis and/or accelerating MΦ clearance of NET could provide, along with NET monitoring in blood, new approaches for treating infections and polymorphonuclear neutrophil (PMN)-mediated tissue damage[13] that involve pathologic NETosis.

Because SARS-CoV-2 infections are associated with excess inflammation and coagulopathies associated with NETs, we investigated whether each of the new RvTs could regulate NET formation in human blood ex vivo by using a microfluidic NET-capturing device and with isolated human PMNs as well as in vivo with *Staphylococcus aureus* infection in mice. These results support new resolution functions of the RvTs in reducing NETs and stimulating MΦ clearance of NETs.

Materials and methods

Authentication of the RvTs

The 13-series resolvins RvT1 to RvT4 were each prepared by total organic synthesis as previously described.[22,23] For the current study, before all experiments and for authentication, the integrity of each RvT was assessed by using UV spectroscopy and liquid chromatography/tandem mass spectrometry (LC-MS/MS) to obtain retention times, UV and diagnostic MS/MS spectra to compare with original documentation.[19] Details regarding LC-MS/MS equipment and conditions, mass spectrum, and the UV spectrum of each synthetic RvT are presented in supplemental Figure 1 (available on the *Blood* Web site).

Human blood NETosis and quantification: microfluidic NET-capturing devices

Human peripheral blood was drawn from healthy volunteers (Mass General Brigham investigational review board protocol no. 1999-P-001297) by venipuncture with sodium heparin (BD Vacutainer). Aliquots of blood (500 μL) were incubated with 10 nM RvT1 to RvT4 (supplemental Figure 1), resolvin D2 (RvD2), leukotriene B_4 (LTB_4; purchased from Cayman Chemicals, Ann Arbor, MI), or vehicle control (0.01% ethanol v/v) in saline at 37°C for 15 minutes, followed by the addition of phorbol 12-myristate 13-acetate (PMA; 1 μg/mL; Cayman Chemicals). After incubations for 4 hours, 50 μL of blood was added to 450 μL of Sytox Green or Sytox Orange (5 μM; Thermo Fisher Scientific, Waltham, MA) for 15 minutes, then loaded onto the NET-capturing devices[†] (Figure 1) and drawn through the postarrays. NETs captured within the postarrays were then imaged with an

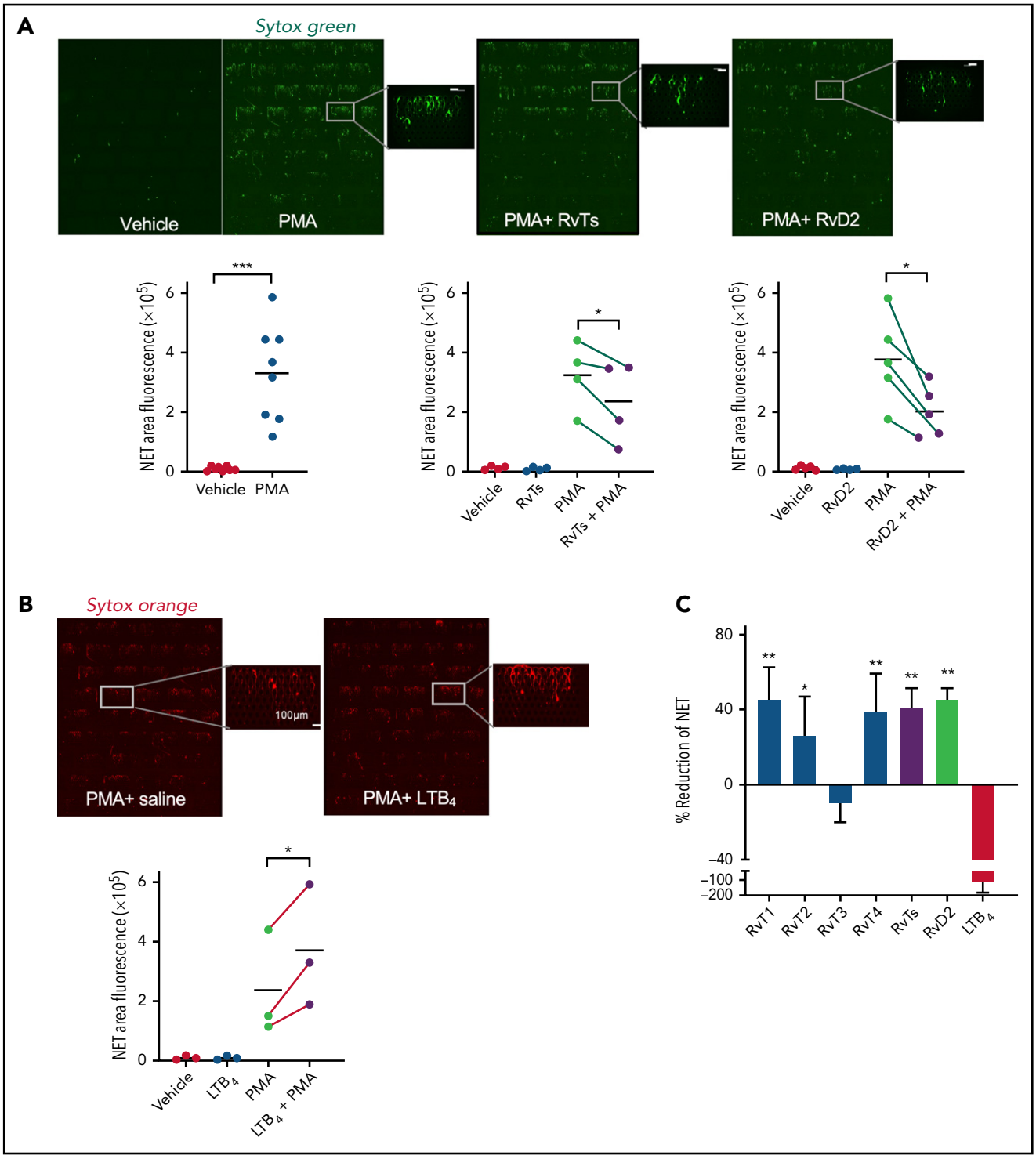

Figure 2. RvTs reduce NETs in human peripheral blood. Human blood (500 μL) was incubated with RvT1, RvT2, RvT3, and RvT4 (10 nM each) individually, or with a combination of RvTs (RvT1-RvT4; 2.5 nM each), RvD2 (10 nM), LTB_4 (10 nM), or vehicle control (0.01% ethanol v/v in saline) at 37°C for 15 minutes followed by the addition of PMA (1 μg/mL) for 4 hours. Aliquots of blood (50 μL) were added to Sytox Green (450 μL) and loaded onto the inlet reservoirs of the microfluidic NET devices. NETs captured within the micropost arrays were then imaged and quantified. (A) (Top panels) Representative images of fluorescent NETs using Sytox Green. Scale bars = 100 μm. (Bottom panels) Results are expressed as NET areas. The NET areas of PMA and PMA plus RvTs or RvD2 obtained from the same donors are connected by green lines. n = 4 (RvTs) or n = 5 (RvDs) separate donors. $*P < .05$, $***P < .001$, paired two-tailed Student *t* test. (B) (Top panels) Representative images of fluorescent NETs using Sytox Orange. Scale bars = 100 μm. (Bottom panel) The NET areas of PMA and PMA plus LTB_4 obtained from the same donors are connected by red lines. n = 3 separate donors. $*P < .05$, paired two-tailed Student *t* test. Details on imaging and quantification are given in the "Materials and methods." (C) Results are percent reduction of NETs compared with PMA alone. Mean ± SEM. n = 3 to 5. $*P < .05$, $**P < .01$, vs LTB_4.

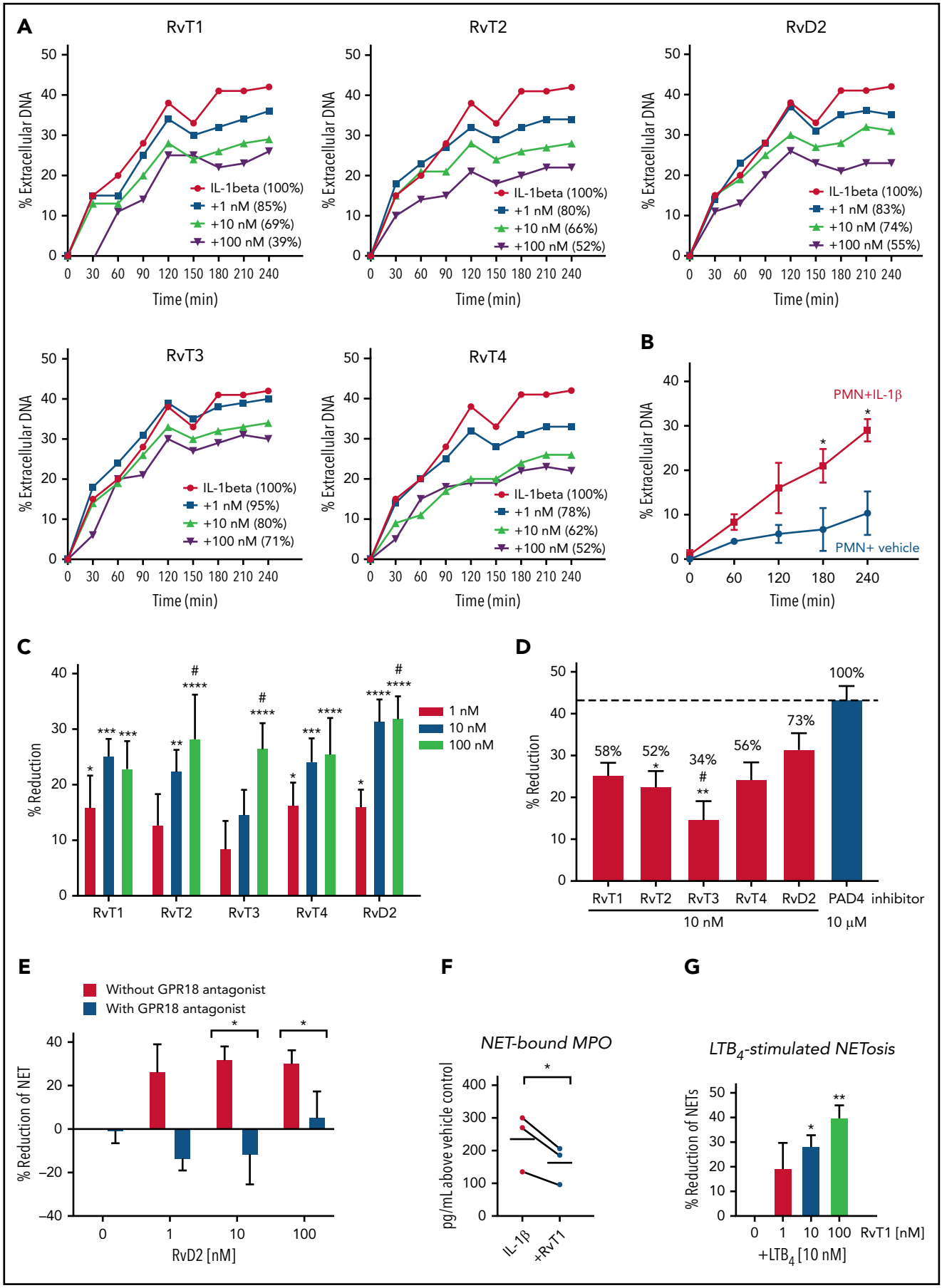

Figure 3. RvTs reduce NETs with isolated human PMNs. Freshly isolated human PMNs were incubated with test compounds RvT1, RvT2, RvT3, RvT4, and RvD2 (1-100 nM) or vehicle control (0.01% ethanol v/v) at 37°C for 15 minutes, followed by the addition of IL-1β (50 ng/mL) with Sytox Green (5 μM). Fluorescence was

automated Nikon TiE microscope (Micro Device Instruments, Calabasas, CA). The amounts of NETs captured within the devices were quantified by using fluorescent dyes binding to strings of extracellular chromatin. For human blood samples, we quantified the total area of fluorescent entities with an area >100 μm^2 (to exclude nuclear staining) and a shape factor in the circularity range of 0 to 0.5 using ImageJ software (version 2.0.0-rc-69/1.52p; National Institutes of Health, Bethesda, MD). The chromatin fibers were verified to be NETs by using specific antibodies against citrullinated histone H3. The design and construction of the microfluidic NET device will be reported elsewhere (Miyuki Sakuma, Xiao Wang, Felix Ellett, Jon Edd, Babatunde Kehinde, Adam Viens, Michael K. Mansour, and Daniel Irimia, manuscript submitted).

Human PMN isolation and NET formation

Human PMNs were isolated,[37] and viability was determined by using Trypan Blue exclusion. Freshly isolated PMNs were plated onto 96-well plates (1×10^5 cells per well) in NET buffer (RPMI 1640 with 1% bovine serum albumin and 1 mM calcium chloride). Resolvins, including RvD2, RvT1, RvT2, RvT3, and RvT4 (1-100 nM), or the peptidylarginine deiminase 4 (PAD4) inhibitor GSK484 hydrochloride (10 μM; Cayman Chemicals), or vehicle control (0.01% ethanol v/v) were incubated with PMNs at 37°C for 15 minutes, followed by the addition of IL-1β (50 ng/mL; Miltenyi Biotec, Gaithersburg, MD) with Sytox Green (5 μM). In select experiments, GPR18 antagonist O-1918 (20 μM; Abcam, Cambridge, MA) was incubated with PMNs for 10 minutes before the addition of RvD2. Fluorescence was monitored for 0 to 4 hours by using a SpectraMax M3 plate reader (Molecular Devices, San Jose, CA). At 4 hours, Triton X-100 (0.5%; Sigma-Aldrich) was added to lyse the cells to determine fluorescence from total DNA. NETs (percent extracellular DNA) were calculated as: [(fluorescence at 1, 2, 3, or 4 hours) – (fluorescence at 0 hour)]/[(fluorescence at 4 hours after lysis with Triton X-100) – (fluorescence at 0 hour)] × 100%. Details regarding measurement of myeloperoxidase (MPO) and preparation of human NETs for MΦ phagocytosis are presented in the supplemental Methods.

S aureus infection in murine dorsal air pouches

Animal experimental procedures were approved by the Institutional Animal Care and Use Committee of Brigham and Women's Hospital (protocol no. 2016N000145). Dorsal air pouches were raised for 6 days.[38] Mice were given a panel of RvTs (RvT1, RvT2, RvT3, and RvT4; 50 ng each) or vehicle control with live *S aureus* (serotype [b]c1; 10^7 colony-forming units [CFU]) by intra-pouch injection. Sixteen hours later, the mice were euthanized, and intra-pouch exudates were collected. Information on determination of total leukocytes, PMNs, bacterial titers, and NETs is presented in the supplemental Methods.

Immunofluorescence staining

Immunostainings were performed in 8-well chamber slides and images captured by using a BIOREVO BZ-9000 (Keyence, Osaka, Japan) inverted fluorescence phase-contrast microscope equipped with a monochrome/color switching camera with BZ-II Viewer software (Keyence). Information on staining conditions and antibodies used is presented in the supplemental Methods.

Human MΦ preparation and ingestion of NETs

Human peripheral blood mononuclear cells were obtained from the Boston Children's Hospital Blood Bank (Mass General Brigham investigational review board protocol #1999-P-0001297). Peripheral blood mononuclear cells were isolated for preparation of M0-MΦ, M1-MΦ, and M2-MΦ (supplemental Methods).[39] MΦs were plated onto 8-well chamber slides (1×10^5 cells per well in RPMI 1640 supplemented with 10% FBS) overnight. The next day, RvD2, RvT1 to RvT4 (10 nM), or vehicle controls were added to MΦs for 15 minutes, followed by the addition of Sytox Green–labeled NETs. NETs from 1×10^6 PMNs (~10 μg DNA) were added to 1×10^5 MΦs for 1 hour. Supernatants were removed and cells fixed in 4% paraformaldehyde. In select experiments, MΦs were incubated with a PKA inhibitor (H89, 3 μM for 24 hours; Sigma-Aldrich) or an AMP-activated protein kinase (AMPK) inhibitor (Compound C, 500 nM for 4 hours; Sigma-Aldrich) before addition of RvT2 (10 nM) and NETs. Images were then acquired by using a Keyence BZ-9000 fluorescence microscope and quantified by using BZ-II Viewer software (Keyence). Cells were also stained with PKH26 Red (MilliporeSigma, St. Louis, MO) for representative images. For cyclic adenosine monophosphate (cAMP), human MΦs were incubated with RvT2 (1-100 nM) or vehicle control (0.1% ethanol v/v in Dulbecco's phosphate-buffered saline with Ca^{2+} and Mg^{2+}DPBS++) for 15 minutes and cAMP determined by using enzyme-linked immunosorbent assay (Cayman Chemicals).

Mouse peritoneal MΦ ingestion of NETs in vivo

Mice were given zymosan (1 mg/mL, intraperitoneally [IP]) for 72 hours to elicit MΦs, followed by administration of RvT2 (100 ng/mL per mouse, IP) or vehicle (0.05% v/v ethanol) for 15 minutes, and NETs (from ~10×10^6 PMNs) for 60 minutes. Exudate cells (2×10^5 cells) were adhered onto 8-well chamber slides for imaging and quantification of green fluorescence associated with cells.

Statistical analysis

Statistical analyses were performed by using two-tailed Student *t* tests for 2-group comparisons or one-way analysis of variance with multiple group comparisons for ≥3 independent groups

Figure 3 (continued) monitored from 0 to 4 hours. (A-B) Dose response and time course of NETosis. The fluorescence of extracellular DNA in the presence of IL-1β alone was taken as 100%. The percentages of extracellular DNA in the presence of test compounds (1-100 nM) at 4 hours are indicated in parentheses. (A) One representative from 7 separate donors. (B) Mean ± SEM. n = 3 separate donors. *$P < .05$, vs PMN + vehicle. (C) Dose response of each RvT and RvD2. Results are expressed as percent reduction compared with IL-1β alone at 4 hours. Mean ± SEM. n = 7 separate donors. *$P < .05$, **$P < .01$, ***$P < .001$, ****$P < .0001$, vs 0 nM; $^{\#}P < .05$, vs 1 nM (two-way analysis of variance with Tukey's multiple comparisons). (D) Comparison of SPMs (10 nM) and a PAD4 inhibitor (10 μM). Numbers shown on top of each bar are percentages compared with the PAD4 inhibitor that was taken as 100%. Mean ± SEM. n = 7 (SPMs) or n = 3 (inhibitor) separate donors. *$P < .05$, **$P < .01$, vs PAD4 inhibitor; $^{\#}P < .05$, vs RvD2 (one-way analysis of variance with Tukey's multiple comparisons). (E) GPR18-dependent RvD2 action. PMNs were incubated with a GPR18 antagonist. O-1918 (20 μM) for 10 minutes before the addition of RvD1 (1-100 nM) and/or IL-1β. Mean ± SEM. n = 3 separate donors. *$P < .05$, two-tailed Student *t* test. (F) MPO levels. PMNs were incubated with RvT1 (10 nM) or vehicle control at 37°C for 15 minutes, followed by the addition of IL-1β (50 ng/mL) for 4 hours. DNA (NET)-bound MPO was determined. MPO levels from the same donors are connected by black lines. n = 3 separate donors. *$P < .05$. (G) LTB_4-stimulated NETosis. PMNs were incubated with RvT1 (1-100 nM) or vehicle control at 37°C for 15 minutes, followed by the addition of LTB_4 (10 nM) with Sytox Green (5 μM). Fluorescence was monitored at 4 hours. Mean ± SEM. n = 3 separate donors. *$P < .05$, **$P < .01$, vs LTB_4 alone and LTB_4 + 1 nM RvT1.

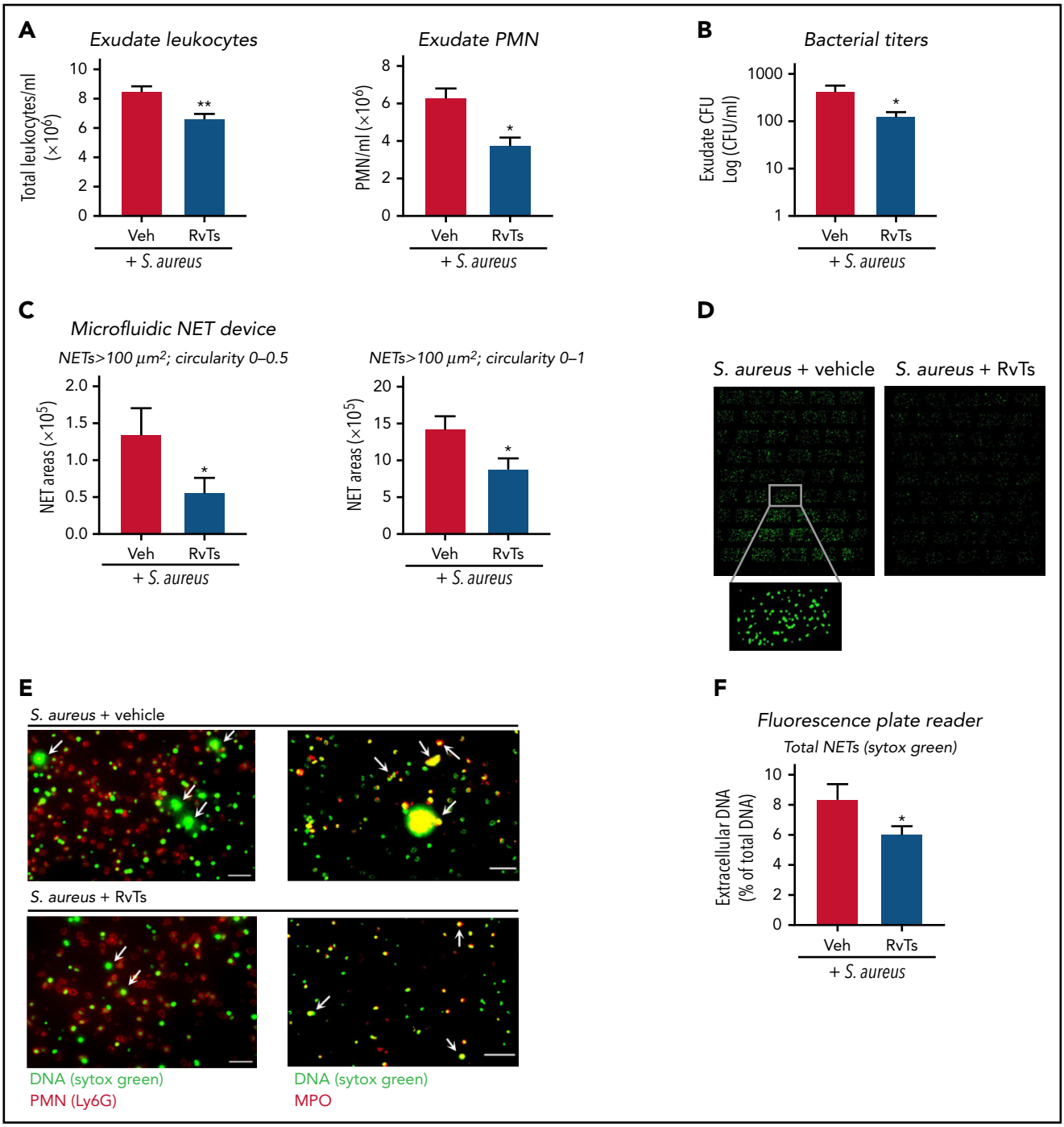

Figure 4. RvTs limit *S aureus* infection and reduce NETs in vivo. Mice were given a panel of RvTs (RvT1, RvT2, RvT3, and RvT4; 50 ng each) or vehicle control together with live *S aureus* (10^7 CFU) by intra-pouch injection. Sixteen hours later, pouch exudates were collected. (A) Exudate leukocytes were enumerated by using light microscopy and PMN percentages determined by differential counting. Mean ± SEM. n = 7 (leukocytes) or n = 4 (PMNs). *$P < .05$, **$P < .01$, two-tailed Student *t* test. (B) Exudate bacterial titers were determined by enumerating colonies on LB agar plates. Mean ± SEM. n = 6. *$P < .05$, two-tailed Student *t* test. (C) NETs were quantified by using the microfluidic NET devices. Exudate cells (2×10^5 cells) were incubated with Sytox Green (5 μM) for 15 minutes and loaded onto the microfluidic NET device. NETs were quantified according to 2 criteria: (left) long-string NETs > 100 μm^2 (fluorescent areas larger than 100 μm^2 in size with a shape circularity 0-0.5) or (right) NETs > 100 μm^2 (fluorescent areas larger than 100 μm^2 in size with shape circularity 0-1). Mean ± SEM. n = 5 or 6. *$P < .05$, two-tailed Student *t* test. (D) Representative images of NETs > 100 μm^2 and shape circularity 0-1. (E) Representative images. Exudate cells (2×10^5 cells) were adhered onto 8-well chamber slides, incubated with Sytox Green (5 μM), followed by staining with (left panels) phycoerythrin-conjugated anti-Ly6G antibody for mouse PMN or (right panels) goat anti-mouse MPO antibody. Arrows denote NETs. Scale bars = 50 μm. (F) NETs were quantified by using a fluorescence plate reader. Exudate cells (1×10^5 cells) were adhered onto a 96-well plate, incubated with Sytox Green (5 μM) for 20 minutes, and fluorescence determined. Mean ± SEM. n = 7. *$P < .05$, two-tailed Student *t* test. Veh, vehicle control.

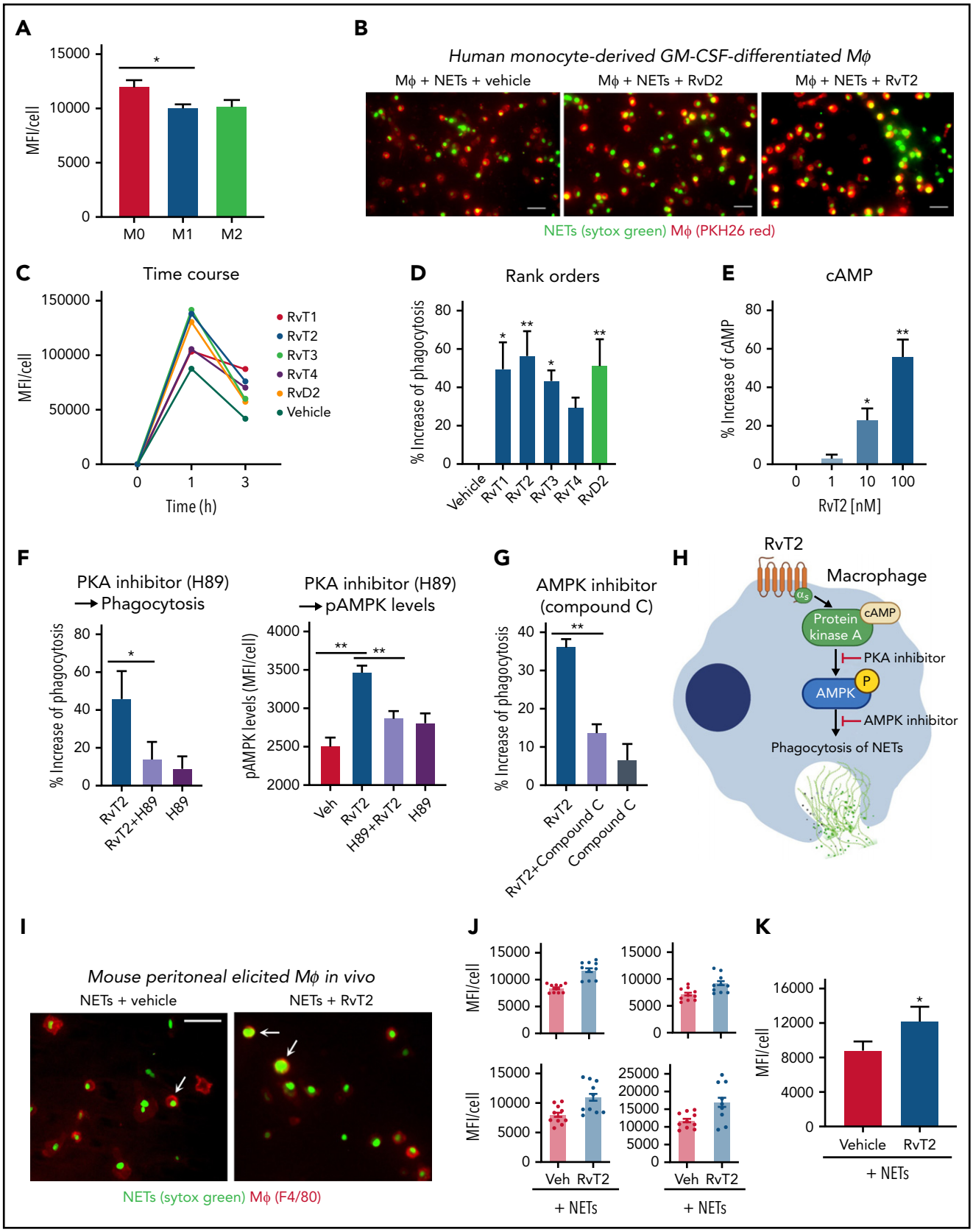

Figure 5. RvTs enhance MΦ ingestion of NET in vitro and in vivo. (A-D) Human MΦs were plated onto 8-well chamber slides (1×10^5 cells per well). Test compounds (RvT1-RvT4, RvD2; 10 nM) or vehicle controls were added to MΦs for 15 minutes, followed by the addition of Sytox Green–labeled NETs for 1 hour. NETs from ~1×10^6 PMNs (~10 μg DNA) were added to 1×10^5 MΦs per well. (A) Mean fluorescence intensity (MFI) per cell with M0-MΦ, M1-MΦ, and M2-MΦ. Mean ± SEM. n = 3 separate donors. *$P < .05$. (B) Representative images of M0-MΦs (PKH26 Red) with ingested Sytox Green–labeled NETs. Scale bars = 50 μm. (C-D) An average

(GraphPad Prism; GraphPad Software, La Jolla, CA and Microsoft Excel; Microsoft Corporation, Redmond, WA). P values $< .05$ were taken as significant.

Informed consent was obtained from each volunteer in accordance with the Declaration of Helsinki.

Results

RvTs reduce NETosis in human blood

We investigated whether RvTs regulate NETosis by screening them in human heparinized whole blood using a novel microfluidic NET device.* RvT structures used in this screen are shown in Figure 1A. The microfluidic NET-capturing devices were designed and constructed on glass slides with multiple arrays of posts, as shown in Figure 1B. The devices capture NETs mechanically within the arrays of posts directly from human blood without the need to isolate PMNs* (also discussed in the "Materials and methods"). Because the four RvTs were identified in peripheral human blood[19] and biosynthesized from a central transient intermediate (namely 7S-hydroperoxy-13R-hydroxy-8E,10Z,14E, 16Z,19Z-docosapentaenoic acid) to essentially equivalent amounts of the four bioactive products (Figure 1A; supplemental Figure 1A), they may act in concert intraluminally in blood. To test this theory, we first used a mixture of four RvTs (2.5 nM each, total of 10 nM). Freshly drawn human blood (500 μL) was incubated with the RvTs (2.5 nM each), RvD2, or LTB_4 (10 nM each) for direct comparisons, or vehicle control (0.01% ethanol v/v) in saline at 37°C for 15 minutes, followed by the addition of PMA (1 μg/mL), an established NETosis agonist,[28] for 4 hours at 37°C. The integrity of each of the four RvTs was authenticated by monitoring their physical properties using targeted LC-MS/MS and UV spectroscopy before the experiments (supplemental Figure 1B-E). The NETs in blood were stained by using double-stranded DNA–binding fluorescent dye Sytox Green, loaded onto the microfluidic devices and captured within the arrays of posts. NETs were automatically identified in fluorescence images based on their "long-string" features (circularity 0-0.5 and total area >100 μm^2). The total area of NETs in each device was quantified. PMA markedly and consistently increased the measured total NET areas, which were significantly reduced by the RvTs, added together at nanomolar amounts to human blood, by >30% (Figure 2A).

For direct comparisons, we tested RvD2 because of its proven potent immunoresolvent properties in controlling septic infections and septic burn wounds[15,40,41]; RvD2 also significantly decreased NETs by 45.4 ± 5.2% (Figure 2A). Neither RvTs nor RvD2 alone increased NETs captured from human blood. In contrast, the proinflammatory LTB_4 at equi-molar concentrations significantly increased PMA-stimulated NETs by 116.0 ± 53.0% compared with PMA alone as an NETosis agonist, quantified by using Sytox Green, and representative images taken by using Sytox Orange (Figure 2B). Each RvT (RvT1, RvT2, RvT3, and RvT4 at 10 nM) was tested separately. Compared with LTB_4, which increased NETs, RvT1, RvT2, and RvT4 each produced a trend to reduce PMA-stimulated NETs; RvT1, RvT2, and RvT4 separately or together were significantly different from LTB_4 ($P < .05$) (Figure 2C). Here, RvT3 did not yield an apparent reduction in PMA-stimulated NETs in human blood. Thus, we showed that select resolvins reduced NETs, whereas LTB_4 heightened NETs using a microfluidic NET-capturing device in human blood.

RvTs decrease NETosis with isolated human PMNs

We next sought evidence for the direct action of RvTs on PMNs. Because RvTs block activation of inflammasome components (including IL-1β),[19] and inflammasome activation is known to be involved in COVID-19 severity,[42] we used IL-1β as the stimulus for NETosis. IL-1β and NETs constitute a positive feed-forward loop that accelerates aberrant human immune responses in severe COVID-19.[34] Given these lines of evidence, we interrogated each RvT separately to examine their potential to regulate IL-1β–stimulated NETs using freshly isolated human PMNs. For these, we determined their kinetics, dose responses, and rank order potencies. Freshly isolated human PMNs (>95% viability, n = 7) were incubated with RvT1, RvT2, RvT3, and RvT4 separately (1-100 nM) or vehicle control at 37°C for 15 minutes, followed by the addition of IL-1β (50 ng/mL) with Sytox Green for 4 hours. In these experiments, dead PMNs comprised <10% of total PMNs (n = 3). Time courses and dose response of NET release were determined by using a fluorescence plate reader (Figure 3A-B). IL-1β (50 ng/mL) significantly increased NETosis from 3 to 4 hours compared with vehicle controls (Figure 3B); representative images at 4 hours are shown in supplemental Figure 2. RvT1 to RvT4 each dose dependently reduced NETosis from 1 to 100 nM (Figure 3C); the time course of a representative donor is shown in Figure 3A. Histone citrullination by PAD4 is involved in chromatin decondensation and NET formation; blockage and/or deletion of PAD4 is known to reduce NETosis.[31,43,44] Thus, a PAD4 inhibitor was used as a positive control for direct comparison (Figure 3D). At 10 nM, RvT1, RvT2, and RvT4 each provided ~58%, ~52%, and ~56% potencies, directly compared with a PAD4 inhibitor (GSK484 hydrochloride 10 μM; taken as 100%). By comparison, RvT3 (~34% of PAD4 inhibitor) was significantly less potent than RvD2.

Figure 5 (continued) of ~300 MΦs were quantified in each condition for each donor. (C) Time course of MFI per MΦ: a representative donor from n = 4 separate donors. (D) Results are percent increase of MFI/MΦ compared with MΦ + NET + vehicle. Mean ± SEM. n = 8 separate donors. *$P < .05$, **$P < .01$, one-way analysis of variance with Tukey's multiple comparisons. (E) cAMP. Human M0-MΦs (1×10^5/0.2 mL) were incubated with RvT2 (0-100 nM) for 15 minutes. MΦs were lysed and cAMP levels determined. Results are percent increase above vehicle. Mean ± SEM. n = 3. *$P < .05$, **$P < .01$, vs vehicle. (F-G) Human M0-MΦs (1×10^5 cells/well in 8-well chamber slides) were incubated with RvT2 (10 nM), a PKA inhibitor (H89, 3 μM, 24 hours), the AMPK inhibitor (Compound C, 500 nM, 4 hours), or vehicle controls for 15 minutes, followed by the addition of Sytox Green–labeled NETs for 1 hour. MΦ ingestion of NETs was quantified according to Sytox Green intensities and pAMPK levels quantified according to immunofluorescence with an anti–phospho-AMPK (pAMPK) antibody. Mean ± SEM. n = 5 (phagocytosis) or n = 3 (pAMPK levels) separate donors. *$P < .05$, **$P < .01$. (H) Proposed RvT2-cAMP-PKA-AMPK axis in stimulating MΦ phagocytosis of NETs. (I-K) Mice were given zymosan (1 mg/mL, IP) for 72 hours, followed by RvT2 (100 ng/mL per mouse, IP) or vehicle (0.05% ethanol) for 15 minutes, and fluorescent-labeled NETs (~100 μg/mL DNA from ~10×10^6 PMN) for 60 minutes. Exudate cells (2×10^5 cells) were adhered onto 8-well chamber slides for imaging and quantification. An average of ~780 MΦs was quantified per condition per mouse. (I) Representative images of MΦs (red: F4/80) with ingested Sytox Green–labeled NETs, denoted by arrows. Scale bars = 50 μm. (J) Four independent experiments and 4 mice each group. In each experiment, 10 fields (20×) per mouse were imaged and quantified. (K) Mean ± SEM from n = 4. *$P < .05$, two-tailed paired Student t test. GM-CSF, granulocyte-macrophage colony-stimulating factor; Veh, vehicle control.

Thus, RvTs shared the potent NET-reducing actions of RvD2 (10 nM), providing ~70% potencies compared with a PAD4 inhibitor (10 μM).

Earlier, we identified a specific cell surface G protein–coupled receptor (GPCR) for RvD2-denoted GPR18 that mediates the functions of RvD2 in enhancing PMN and MΦ phagocytosis to control bacterial infections.[45] Figure 3E presents the results for RvD2 and the contribution of its GPCR to NETosis. The RvD2 receptor antagonist O-1918 alone did not significantly alter IL-1β–stimulated NETs; when incubated together with RvD2 (10-100 nM), O-1918 significantly diminished the ability of RvD2 to reduce NETosis ($P < .05$).

Among the 4 synthetic RvTs, RvT1 was apparently the most potent in reducing NETosis with human PMNs; it was thus selected for further investigations. Because MPO is a critical component for NET formation,[46] we assessed PMN-released NET-bound MPO. IL-1β stimulation increased NET-bound MPO, which was significantly reduced by RvT1 (10 nM) by ~30% (Figure 3F). These results indicate that RvTs reduced critical components of NET assembly (ie, extracellular DNA and MPO).

We next questioned whether RvT1 regulates the proinflammatory lipid mediator LTB_4-stimulated NETosis and found that RvT1 dose dependently (1-100 nM) reduced LTB_4-triggered NETosis, giving 30% to 40% reduction at 10 to 100 nM (Figure 3G). RvT1 (10-100 nM) did not activate recombinant human BLT1, a specific receptor for LTB_4,[47] nor did it antagonize LTB_4 signals via BLT1 (supplemental Figure 3). Similar results were obtained for RvT2, RvT3, and RvT4, indicating that RvTs do not interact with human BLT1. Taken together, these results obtained with both human blood and isolated PMNs revealed the potent new actions of each RvT and RvD2 in reducing NETosis. The largest share of the RvD2 mechanism was mediated by its cell surface receptor, suggesting that the RvTs may each also interact with specific cell surface receptors on human phagocytes. This could explain the potent actions of each RvT at low nanomolar ranges on PMNs (Figure 3) and MΦs (discussed earlier).

RvTs control *S aureus* infection and reduce NETs in vivo

To investigate RvT actions in vivo in controlling infection and NETosis, we initiated an *S aureus* infection in a murine dorsal air pouch. *S aureus* is a well-established stimulus for NETosis in vivo.[25] Mice were given a panel of RvTs (RvT1, RvT2, RvT3, and RvT4; 50 ng each) or vehicle control together with live *S aureus* (10^7 CFU) by intra-pouch injection. Exudates were collected at 16 hours. *S aureus* induces NET formation that did not require neutrophil lysis.[48] We verified that the bacterial titers used here (10^7 CFU) gave low percentages of cell death, and no statistically significant differences were obtained between vehicle- and RvT-treated mice (~3.2% vs ~3.8% dead cells). RvTs, when given together with *S aureus*, significantly reduced exudate PMN numbers by ~40% and bacterial titers by ~70%, compared with *S aureus* plus vehicle control (Figure 4A-B; supplemental Figure 4A). Exudate cells were stained with Sytox Green, and NETs were quantified by using both microfluidic NET-capturing devices and a fluorescence microplate reader. Using NET-capturing devices, the long-string NETs with an area larger than 100 μm^2 and a shape factor in the circularity 0 to 0.5 range were first quantified. Exudates from RvT-treated mice contained ~60% less long-string NETs compared with vehicle-treated mice ($P < .05$) (Figure 4C). Long-string NETs comprised ~10% of the extracellular fluorescent chromatin in all shapes (>100 μm^2; circularity 0-1). Thus, we also compared the amount of extracellular chromatin in all shapes and found a statistically significant smaller amount in RvT-treated mice compared with vehicle-treated mice ($P < .05$) (Figure 4C-D). We verified that the chromatin was neutrophil derived by staining for MPO (Figure 4E). PMNs were labeled with phycoerythrin-conjugated anti-Ly6G antibody, and NETs were labeled with anti-MPO antibody and/or Sytox Green (supplemental Figure 4B). These results are in line with those determined by using a microplate reader, in which exudate cells from RvT-treated mice produced a statistically significant reduction of NETs ~30% compared with vehicle-treated mice ($P < .05$) (Figure 4F). Together, these results showed that, in *S aureus*–initiated dermal infection, RvTs potently limited PMN infiltration and reduced bacterial titers, as well as attenuated NETs.

RvTs enhance MΦ clearance of NETs

Human monocyte–derived MΦs can engulf NETs in an active endocytic process that does not induce proinflammatory cytokine secretion.[49] The impaired clearance of NETs by MΦs is associated with sustained inflammation in diseases such as ARDS.[36,50] Because RvTs stimulate MΦ phagocytosis of bacteria and apoptotic PMNs,[19] we investigated whether RvTs can also regulate MΦ uptake of NETs. We first examined human monocyte–derived MΦs of the M0, M1, and M2 phenotypes for their capacity in ingestion of NETs. Fluorescent (Sytox Green)–labeled human NETs were incubated with M0-MΦ, M1-MΦ, or M2-MΦ for 1 hour, and M0-MΦs yielded the highest fluorescence intensity, representing the highest capacity among the three MΦ phenotypes in engulfing NETs (Figure 5A). Thus, M0-MΦs were selected for further investigations. Next, the M0-MΦs were incubated with each RvT separately (10 nM each), followed by the addition of Sytox Green–labeled NETs and PKH26; representative images are shown in Figure 5B. Presented for a representative donor, MΦs ingested fluorescent-labeled NETs in a time-dependent manner; this action was further enhanced with the addition of each RvT separately (Figure 5C). RvT2 was the most potent among the 4 RvTs, giving 56.6 ± 11.9% increase in MΦ ingestion of NETs ($P < .01$) (Figure 5D) at 1 hour, followed in potency by RvT1 and RvT3 ($P < .05$). RvT4 also increased uptake of NETs 29.5 ± 4.8%, although this did not reach statistical significance compared with MΦs incubated with vehicle control. For a direct comparison, RvD2 was essentially as equipotent as RvT2, yielding 51.4 ± 12.9% increases in MΦ uptake of NETs ($P < .01$).

We next examined the molecular targets and intracellular signals for RvT-stimulated phagocytosis of NETs; we selected RvT2 for these studies because it apparently ranked higher than other RvTs in potencies. Because the cAMP-PKA axis contributed to RvD2- and MaR1-stimulated MΦ phagocytosis of *E coli*,[15] we questioned whether RvT2 also activates this axis in enhancing MΦ phagocytosis of NETs. Here, RvT2 (1-100 nM) dose dependently increased cAMP, and the PKA inhibitor H89 diminished RvT2-stimulated phagocytosis (Figure 5E-F), indicating the involvement of cAMP-PKA activation in phagocytosis of NETs. Because activation of AMPK in MΦs improves NET clearance,[36] we investigated whether RvT2 regulated phosphorylation of

AMPK and found that RvT2 (10 nM) significantly increased phospho-AMPK during phagocytosis of NETs, which was abolished by H89, the PKA inhibitor (Figure 5F). Along these lines, the AMPK inhibitor (Compound C) (Figure 5G) significantly reduced RvT2-stimulated MΦ ingestion of NETs. Taken together, these findings indicate that RvT2 activated the cAMP-PKA-AMPK pathway, which contributes to clearance of NETs by human MΦs (Figure 5H).

We sought in vivo evidence of this new RvT function. Peritoneal MΦs were elicited by intraperitoneal injection of zymosan for 72 hours. RvT2 (100 ng/mouse, IP) or vehicle control was given 15 minutes before Sytox Green–labeled NETs for 1 hour and exudates collected for single-cell resolution imaging and quantification. RvT2 significantly increased fluorescence associated with exudate MΦs by 37.3 ± 3.4% ($P < .05$) (Figure 5I-K), representing enhanced MΦ ingestion of NETs compared with vehicle controls. These results obtained from mouse peritoneal MΦs were consistent with those from human MΦs with RvT2 (Figure 5A-H). Together, results obtained from both human and mouse MΦs uncovered a new pro-resolving function of specific RvTs, such as RvT2; that is, stimulating human MΦ clearance of NETs.

Discussion

In the current report, we identified new resolution functions of RvTs in regulating NET formation and clearance using the 4 novel stereochemically defined RvTs. RvT biosynthesis is initiated via cyclooxygenase-2 and enhanced by atorvastatin, which nitrosylates cyclooxygenase-2.[19] Interestingly, in-hospital use of statins is associated with a reduced risk of mortality in patients with COVID-19 (relative risk, 0.54),[51] and atorvastatin has been proposed as an adjuvant therapy for COVID-19.[52] Thus, in view of our results, it is possible that RvTs contribute to the potential benefits of atorvastatin in reducing mortality in COVID-19.

It is known that COVID-19 pathologies consist of heightened inflammation of respiratory and cardiovascular systems (ie, cytokine storms)[33,42,53] in which leukocytes can undergo NETosis.[32,34] IL-1β–induced NETosis accelerates aberrant immune responses in severe COVID-19 via an inflammatory loop.[34] An IL-1β receptor antagonist was recently launched for clinical trials for COVID-19 (ClinicalTrials.gov identifiers #NCT04324021 and #NCT04330638). In addition to cytokine storms, inflammatory lipid mediators are identified in COVID-19. Patients with severe COVID-19 and nonsurvivors have increased pro-inflammatory lipid mediators, including LTB_4.[54,55] In this context, pro-resolving mediators, including RvTs, could be useful in controlling COVID-19 disease severity because of their potent anti-inflammatory, pro-resolving, microbial clearance, and organ-protective actions.[15] Both RvD1 and RvD2 limit SARS-CoV-2 spike S1 protein–activated cytokine storms with human MΦs.[10]

In the current experiments, RvTs reduced both IL-1β– and LTB_4-induced NETosis (Figure 3) and enhanced NET uptake by MΦs (Figure 5), which helped to clear NETs in vivo (Figure 4). Recently, resolvins were identified in bronchoalveolar lavages,[54] serum,[11] and plasma[56] from patients with COVID-19. Reduction of resolvin levels, including RvTs, and impairment of phagocyte functions are associated with severe cases of COVID-19 even after resolution of the COVID-19 clinical symptoms; addition of select SPMs restores functions of phagocytes from these patients. Thus, pro-resolving bioactive lipid mediator metabolomes could provide a molecular basis for precision nutrition in SARS-CoV-2 infections and perhaps long-term COVID-19 symptoms.[57]

In human MΦs, RvT2 increased cAMP, a second messenger of $G_{\alpha s}$ protein after GPCR activation and a key signal for phagocyte functions via activating PKA.[58] Thus, RvT actions are likely to be mediated via their own specific cell surface GPCRs that initiate cAMP-dependent pro-resolving intracellular mechanisms to counter pro-inflammatory signals (eg, IL1β and LTB_4). Activation of AMPK in MΦs improves NET clearance,[36] and RvT2 increased phosphorylation of AMPK (Figure 5F-G). Along these lines, RvD1 enhances mouse MΦ uptake of necrotic cells via activation of phospho-AMPK.[59] Our current results, together with earlier findings,[59] emphasize the pro-resolving cAMP-PKA-AMPK axis (Figure 5H) in mediating resolvin-stimulated MΦ functions, including clearance of NETs as well as necrotic cells. Additional molecular targets could also mediate MΦ clearance of NETs (eg, high-mobility group box 1 [HMGB1]). Patients with ARDS have heightened NETosis, associated with increased HMGB1 accumulation, in which blocking HMGB1 improves clearance of NETs by ARDS MΦs.[36] Along these lines, with human monocytes, HMGB1 and C1q regulate the lipid mediator class switching from LT to resolvin production, including RvD1,[18] and RvD1 reduces HMGB1 release in lung injury in mice.[60] Thus, it is possible that RvTs share these protective mechanisms via reducing HMGB1, which contributes to enhanced MΦ clearance of NETs (Figure 5).

RvT1 limited NETs and reduced NET-bound MPO with human PMNs (Figure 3F). In this regard, earlier findings showed that several SPMs, including 15R-LXA_4[16,61] and 17R-RvD1,[62] reduce MPO and/or neutrophil elastase, critical components of NETs, in acute lung injury and lung inflammation. It is noteworthy that these SPMs also reduce NETs in mice in which RvD1 decreases aortic aneurysm via reducing NETs.[63] In deep vein thrombosis, RvD4 attenuates NETs in vivo.[64] Mice deficient in the GPCR denoted ALX (the lipoxin A_4 and RvD1 receptor[15]) exhibit heightened NETosis and lung injury in bacterial pneumonia, in which lipoxin A_4 reduces NETs in an ALX receptor–dependent manner.[65] Taken together, our current results suggest that resolvin pathways (eg, RvDs and RvTs) and their receptors (eg, LXA_4-ALX, RvD2-GPR18, and potentially RvT-specific receptors) could provide new opportunities in managing diseases in which NETosis is a pathological component (eg, SARS-CoV-2 infection [discussed earlier]),[34] lung inflammation/ARDS,[30] and cardiovascular[29] and autoimmune diseases[28] as well as certain cancers.[26]

RvTs limited NETosis initiated by several stimuli, including cytokine (ie, IL-1β) and proinflammatory lipid mediators (ie, LTB_4) that are known to be important in COVID-19[11,34,54] as well as bacteria (*S aureus*) in infection.[25] Our current results indicate that RvTs limit extracellular NETs and MPO (Figures 2-4) and reduce bacteria titers in infectious inflammatory exudates (Figure 4B). RvTs enhanced MΦ uptake of NETs in vitro and in vivo (Figure 5). Thus, RvTs can promote resolution of inflammation and infection[19] via targeting excessive NETosis without blocking critical host defense mechanisms (eg, phagocytosis). Resolvins in general are not immunosuppressive.[15] As shown herein, this appears to be the case with RvTs as well in that they did not cause immune suppression.

In summary, using the stereochemically defined RvTs and microfluidic NET-capturing devices (Figure 1), we found that RvTs reduced NETs in human blood (Figure 2). These findings were evaluated and proven with IL-1β– and LTB_4-stimulated NETosis and isolated human PMNs (Figure 3). Dose responses and rank order potencies of each synthetic RvT were established with human PMNs. Regarding infections in vivo, RvTs limited *S aureus* dermal infection and attenuated NETs (Figure 4). Together, these results in vitro and in vivo uncovered new resolution mechanisms of RvTs, namely that RvTs regulate both NET formation and NET clearance (Figure 5 and supplemental Figure 5), relevant in infections, coagulopathies,[33] and organ protection. This approach of monitoring NETosis and its regulation by RvT treatment may be useful in long COVID syndromes[66] and other NET-associated human infections and pathologies.[32,34]

Acknowledgments

The authors thank Mary H. Small for expert assistance in manuscript preparations and Robert Nshimiyimana (CET&RI, Brigham and Women's Hospital) for conducting the LC-MS/MS authentication of the synthetic RvTs.

This work was supported in part by the National Institutes of Health, National Institute of General Medical Sciences (R35GM139430 and P01GM095467, C.N.S.), and by Shriners Hospital for Children (grant 85123, D.I.).

Authorship

Contribution: N.C. designed and conducted experiments, acquired and analyzed data, and wrote the manuscript; M.S. constructed microfluidic devices, conducted experiments, and acquired and analyzed data; A.R.R. and B.W.S. synthesized RvTs; D.I. designed microfluidic devices, designed experiments, and analyzed data; C.N.S. conceived the overall research, designed experiments, and wrote the manuscript; and all authors contributed to data and manuscript preparation.

Conflict-of-interest disclosure: The authors declare no competing financial interests.

ORCID profiles: N.C., 0000-0003-1963-1585; M.S., 0000-0001-8560-2331; A.R.R., 0000-0002-4802-2845; B.W.S., 0000-0002-7581-4741; D.I., 0000-0001-7347-2082; C.N.S., 0000-0003-4627-8545.

Correspondence: Charles N. Serhan, Center for Experimental Therapeutics and Reperfusion Injury, 60 Fenwood Rd, Hale Building for Transformative Medicine 3-016, Boston, MA 02115; e-mail: cserhan@bwh.harvard.edu.

Footnotes

Submitted 21 July 2021; accepted 22 November 2021; prepublished online on *Blood* First Edition 23 November 2021. DOI 10.1182/blood.2021013422.

The online version of this article contains a data supplement.

There is a *Blood* Commentary on this article in this issue.

The publication costs of this article were defrayed in part by page charge payment. Therefore, and solely to indicate this fact, this article is hereby marked "advertisement" in accordance with 18 USC section 1734.

REFERENCES

1. Serhan CN, Savill J. Resolution of inflammation: the beginning programs the end. *Nat Immunol*. 2005;6(12):1191-1197.
2. Buckley CD, Gilroy DW, Serhan CN. Proresolving lipid mediators and mechanisms in the resolution of acute inflammation. *Immunity*. 2014;40(3):315-327.
3. Perretti M, Cooper D, Dalli J, Norling LV. Immune resolution mechanisms in inflammatory arthritis. *Nat Rev Rheumatol*. 2017;13(2):87-99.
4. Buchheit T, Huh Y, Maixner W, Cheng J, Ji RR. Neuroimmune modulation of pain and regenerative pain medicine. *J Clin Invest*. 2020;130(5):2164-2176.
5. Van Dyke TE. Pro-resolving mediators in the regulation of periodontal disease. *Mol Aspects Med*. 2017;58:21-36.
6. Panigrahy D, Gilligan MM, Serhan CN, Kashfi K. Resolution of inflammation: an organizing principle in biology and medicine. *Pharmacol Ther*. 2021;227:107879.
7. Bäck M, Yurdagul A Jr, Tabas I, Öörni K, Kovanen PT. Inflammation and its resolution in atherosclerosis: mediators and therapeutic opportunities. *Nat Rev Cardiol*. 2019;16(7):389-406.
8. Mirakaj V. Immune cells – a curse and a blessing! *J Exp Med*. 2021;218(6):e20210590.
9. Russell CD, Schwarze J. The role of pro-resolution lipid mediators in infectious disease. *Immunology*. 2014;141(2):166-173.
10. Recchiuti A, Patruno S, Mattoscio D, et al. Resolvin D1 and D2 reduce SARS-CoV-2-induced inflammatory responses in cystic fibrosis macrophages. *FASEB J*. 2021;35(4):e21441.
11. Schwarz B, Sharma L, Roberts L, et al; Yale IMPACT Team. Cutting edge: severe SARS-CoV-2 infection in humans is defined by a shift in the serum lipidome, resulting in dysregulation of eicosanoid immune mediators. *J Immunol*. 2021;206(2):329-334.
12. Serhan CN, Levy BD. Resolvins in inflammation: emergence of the pro-resolving superfamily of mediators. *J Clin Invest*. 2018;128(7):2657-2669.
13. Ward PA, Fattahi F. New strategies for treatment of infectious sepsis. *J Leukoc Biol*. 2019;106(1):187-192.
14. Filep JG. Leukocytes in inflammation, resolution of inflammation, autoimmune diseases and cancer. *Cells*. 2021;10(7):1735.
15. Chiang N, Serhan CN. Specialized pro-resolving mediator network: an update on production and actions. *Essays Biochem*. 2020;64(3):443-462.
16. Sekheri M, El Kebir D, Edner N, Filep JG. 15-Epi-LXA_4 and 17-epi-RvD1 restore TLR9-mediated impaired neutrophil phagocytosis and accelerate resolution of lung inflammation. *Proc Natl Acad Sci USA*. 2020;117(14):7971-7980.
17. Colgan SP. Resolvins resolve to heal mucosal wounds. *Proc Natl Acad Sci USA*. 2020;117(20):10621-10622.
18. Liu T, Xiang A, Peng T, et al. HMGB1-C1q complexes regulate macrophage function by switching between leukotriene and specialized proresolving mediator biosynthesis. *Proc Natl Acad Sci USA*. 2019;116(46):23254-23263.
19. Dalli J, Chiang N, Serhan CN. Elucidation of novel 13-series resolvins that increase with atorvastatin and clear infections. *Nat Med*. 2015;21(9):1071-1075.
20. Walker ME, Souza PR, Colas RA, Dalli J. 13-Series resolvins mediate the leukocyte-platelet actions of atorvastatin and pravastatin in inflammatory arthritis. *FASEB J*. 2017;31(8):3636-3648.
21. Lee CR, Zeldin DC. Resolvin infectious inflammation by targeting the host response. *N Engl J Med*. 2015;373(22):2183-2185.
22. Rodriguez AR, Spur BW. First total syntheses of the pro-resolving lipid mediators 7(*S*),13(*R*),20(*S*)-Resolvin T1 and 7(*S*),13(*R*)-Resolvin T4. *Tetrahedron Lett*. 2020;61(6):151473.
23. Rodriguez AR, Spur BW. First total synthesis of the pro-resolving lipid mediator 7(*S*),12(*R*),13(*S*)-resolvin T2 and its 13(*R*)-epimer. *Tetrahedron Lett*. 2020;61(20):151857.

24. Nauseef WM, Borregaard N. Neutrophils at work. *Nat Immunol*. 2014;15(7):602-611.

25. Kolaczkowska E, Kubes P. Neutrophil recruitment and function in health and inflammation. *Nat Rev Immunol*. 2013;13(3): 159-175.

26. Albrengues J, Shields MA, Ng D, et al. Neutrophil extracellular traps produced during inflammation awaken dormant cancer cells in mice. *Science*. 2018;361(6409): eaao4227.

27. Azcutia V, Parkos CA, Brazil JC. Role of negative regulation of immune signaling pathways in neutrophil function. *J Leukoc Biol*. 2017;103(6):1029-1041.

28. Jorch SK, Kubes P. An emerging role for neutrophil extracellular traps in noninfectious disease. *Nat Med*. 2017;23(3):279-287.

29. Silvestre-Roig C, Braster Q, Ortega-Gomez A, Soehnlein O. Neutrophils as regulators of cardiovascular inflammation. *Nat Rev Cardiol*. 2020;17(6):327-340.

30. Williams GW, Berg NK, Reskallah A, Yuan X, Eltzschig HK. Acute respiratory distress syndrome. *Anesthesiology*. 2021;134(2): 270-282.

31. Wong SL, Wagner DD. Peptidylarginine deiminase 4: a nuclear button triggering neutrophil extracellular traps in inflammatory diseases and aging. *FASEB J*. 2018;32(12): fj201800691R.

32. Nathan C. Neutrophils and COVID-19: nots, NETs, and knots. *J Exp Med*. 2020;217(9): e20201439.

33. Ackermann M, Verleden SE, Kuehnel M, et al. Pulmonary vascular endothelialitis, thrombosis, and angiogenesis in Covid-19. *N Engl J Med*. 2020;383(2):120-128.

34. Barnes BJ, Adrover JM, Baxter-Stoltzfus A, et al. Targeting potential drivers of COVID-19: neutrophil extracellular traps. *J Exp Med*. 2020;217(6):e20200652.

35. Radermecker C, Detrembleur N, Guiot J, et al. Neutrophil extracellular traps infiltrate the lung airway, interstitial, and vascular compartments in severe COVID-19. *J Exp Med*. 2020;217(12):e20201012.

36. Grégoire M, Uhel F, Lesouhaitier M, et al. Impaired efferocytosis and neutrophil extracellular trap clearance by macrophages in ARDS. *Eur Respir J*. 2018;52(2):1702590.

37. Nauseef WM. Isolation of human neutrophils from venous blood. *Methods Mol Biol*. 2014; 1124:13-18.

38. Winyard PG, Willoughby DA, eds. Inflammation protocols. In: Walker JM, ed. Methods in Molecular Biology. Totowa, NJ: Humana; 2003.

39. Dalli J, Serhan CN. Specific lipid mediator signatures of human phagocytes: microparticles stimulate macrophage efferocytosis and pro-resolving mediators. *Blood*. 2012;120(15):e60-e72.

40. Spite M, Norling LV, Summers L, et al. Resolvin D2 is a potent regulator of leukocytes and controls microbial sepsis. *Nature*. 2009;461(7268):1287-1291.

41. Kurihara T, Jones CN, Yu YM, et al. Resolvin D2 restores neutrophil directionality and improves survival after burns. *FASEB J*. 2013;27(6):2270-2281.

42. Rodrigues TS, de Sá KSG, Ishimoto AY, et al. Inflammasomes are activated in response to SARS-CoV-2 infection and are associated with COVID-19 severity in patients. *J Exp Med*. 2021;218(3):e20201707.

43. Martinod K, Demers M, Fuchs TA, et al. Neutrophil histone modification by peptidylarginine deiminase 4 is critical for deep vein thrombosis in mice. *Proc Natl Acad Sci U S A*. 2013;110(21):8674-8679.

44. Veras FP, Pontelli MC, Silva CM, et al. SARS-CoV-2-triggered neutrophil extracellular traps mediate COVID-19 pathology. *J Exp Med*. 2020;217(12):e20201129.

45. Chiang N, Dalli J, Colas RA, Serhan CN. Identification of resolvin D2 receptor mediating resolution of infections and organ protection. *J Exp Med*. 2015;212(8): 1203-1217.

46. Metzler KD, Fuchs TA, Nauseef WM, et al. Myeloperoxidase is required for neutrophil extracellular trap formation: implications for innate immunity. *Blood*. 2011;117(3): 953-959.

47. Yokomizo T, Nakamura M, Shimizu T. Leukotriene receptors as potential therapeutic targets. *J Clin Invest*. 2018; 128(7):2691-2701.

48. Pilsczek FH, Salina D, Poon KK, et al. A novel mechanism of rapid nuclear neutrophil extracellular trap formation in response to Staphylococcus aureus. *J Immunol*. 2010; 185(12):7413-7425.

49. Farrera C, Fadeel B. Macrophage clearance of neutrophil extracellular traps is a silent process. *J Immunol*. 2013;191(5):2647-2656.

50. Haider P, Kral-Pointner JB, Mayer J, et al. Neutrophil extracellular trap degradation by differently polarized macrophage subsets. *Arterioscler Thromb Vasc Biol*. 2020;40(9): 2265-2278.

51. Permana H, Huang I, Purwiga A, et al. In-hospital use of statins is associated with a reduced risk of mortality in coronavirus-2019 (COVID-19): systematic review and meta-analysis. *Pharmacol Rep*. 2021;73(3): 769-780.

52. Ghati N, Roy A, Bhatnagar S, et al. Atorvastatin and aspirin as adjuvant therapy in patients with SARS-CoV-2 infection: a structured summary of a study protocol for a randomised controlled trial. *Trials*. 2020; 21(1):902.

53. Merad M, Martin JC. Pathological inflammation in patients with COVID-19: a key role for monocytes and macrophages [published correction appears in *Nat Rev Immunol*. 2020;20(7):448]. *Nat Rev Immunol*. 2020;20(6):355-362.

54. Archambault AS, Zaid Y, Rakotoarivelo V, et al. High levels of eicosanoids and docosanoids in the lungs of intubated COVID-19 patients. *FASEB J*. 2021;35(6): e21666.

55. Palmas F, Clarke J, Colas RA, et al. Dysregulated plasma lipid mediator profiles in critically ill COVID-19 patients. *PLoS One*. 2021;16(8):e0256226.

56. Koenis DS, Beegun I, Jouvene CC, et al. Disrupted resolution mechanisms favor altered phagocyte responses in COVID-19. *Circ Res*. 2021;129(4):e54-e71.

57. Simopoulos AP, Serhan CN, Bazinet RP. The need for precision nutrition, genetic variation and resolution in Covid-19 patients. *Mol Aspects Med*. 2021;77:100943.

58. Bystrom J, Evans I, Newson J, et al. Resolution-phase macrophages possess a unique inflammatory phenotype that is controlled by cAMP. *Blood*. 2008;112(10): 4117-4127.

59. Hosseini Z, Marinello M, Decker C, et al. Resolvin D1 enhances necroptotic cell clearance through promoting macrophage fatty acid oxidation and oxidative phosphorylation. *Arterioscler Thromb Vasc Biol*. 2021;41(3):1062-1075.

60. Sun Z, Wang F, Yang Y, et al. Resolvin D1 attenuates ventilator-induced lung injury by reducing HMGB1 release in a HO-1-dependent pathway. *Int Immunopharmacol*. 2019; 75:105825.

61. El Kebir D, József L, Pan W, et al. 15-Epi-lipoxin A4 inhibits myeloperoxidase signaling and enhances resolution of acute lung injury. *Am J Respir Crit Care Med*. 2009;180(4):311-319.

62. Wang H, Anthony D, Yatmaz S, et al. Aspirin-triggered resolvin D1 reduces pneumococcal lung infection and inflammation in a viral and bacterial coinfection pneumonia model. *Clin Sci (Lond)*. 2017;131(18):2347-2362.

63. Spinosa M, Su G, Salmon MD, et al. Resolvin D1 decreases abdominal aortic aneurysm formation by inhibiting NETosis in a mouse model. *J Vasc Surg*. 2018;68(6S):93S-103S.

64. Cherpokova D, Jouvene CC, Libreros S, et al. Resolvin D4 attenuates the severity of pathological thrombosis in mice. *Blood*. 2019;134(17):1458-1468.

65. Lefrançais E, Mallavia B, Zhuo H, Calfee CS, Looney MR. Maladaptive role of neutrophil extracellular traps in pathogen-induced lung injury. *JCI Insight*. 2018;3(3):e98178.

66. Fogarty H, Townsend L, Morrin H, et al; Irish COVID-19 Vasculopathy Study (iCVS) investigators. Persistent endotheliopathy in the pathogenesis of long COVID syndrome. *J Thromb Haemost*. 2021;19(10):2546-2553.